UNIVERSIDAD DE CANTABRIA

Departamento de Ingeniería de Comunicaciones

TESIS DOCTORAL

Cryogenic Technology in the Microwave Engineering: Application to MIC and MMIC Very Low Noise Amplifier Design

Juan Luis Cano de Diego

Santander, Mayo 2010

Chapter VII

Subsystems for Radio Astronomy Receivers

Along this thesis different issues concerning the cryogenic technology in the microwaves engineering have been covered. The document started with the design and the assembly of a cryogenic facility that enables all the measurements needed to support the research activity in this field; afterwards, the main measurements techniques used in cryogenics were presented and analyzed completing the basis for this thesis. Finally, the main objective of this thesis was tackled, that is, the design of cryogenic low noise amplifiers: first, the effect of low temperatures in microwave components was investigated in order to finally design MIC and MMIC examples. Now, in this chapter, the circle is completed with a short view to one of the main applications of the cryogenic technology in this field: the receivers for radio astronomy, where the designed LNAs could be implemented.

This chapter starts with a short introduction to some radiometer configurations focusing in their sensitivities and actual implementations. Then, the general scheme of the radiometer designed for the QUIJOTE[1] project is discussed. Finally, since the DICOM has actively participated in the design and measurement of some of the subsystems comprising this radiometer, this work is included at the end of this chapter.

[1] QUIJOTE is a project about radiometers to be installed and operated at Teide observatory (Tenerife, Canary Islands, Spain) aimed for characterizing the CMB polarization as well as to complement data from PLANCK space mission correcting galactic contamination.

7.1. Introduction to Radio Astronomy Radiometers

A radiometer is a highly sensitive receiver designed to measure thermal electromagnetic emission by material media [7.1]. In radio astronomy the objective of the radiometer is to measure the radio emission of celestial sources [7.2]. The signal power level in radio astronomy is quite low with levels often below the noise powers generated in the receiver, therefore a high sensitivity is usually the main requirement in the radiometer design. There are many different radiometer configurations depending on the final application but in most cases they are based on one of the basic structures presented next.

7.1.1. The total power radiometer

A receiver is called total power radiometer if it measures the total noise power from the antenna and from the receiver itself. The basic block diagram of this kind of radiometer is shown in Fig. 7.1. The total power receiver is considered as the basic radiometer since it is comprised of the same parts as more complex receivers and hence the characteristics of these receivers can be deduced from it.

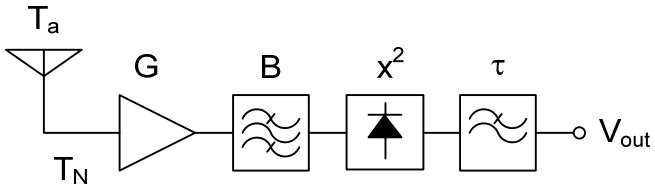

Fig. 7.1. Total power radiometer.

The RF amplifier is probably the most important element in the radiometer. It defines the receiver noise, T_N, and therefore it has a great impact on radiometer sensitivity. In order to improve this sensitivity, this amplifier is often cooled down to cryogenic temperatures resulting in a cryogenic amplifier as those presented in this thesis. The frequency selectivity is defined with a band-pass filter with bandwidth *B*. The detector is of the square-law type which means that the output is a DC voltage directly proportional to the receiver input noise power. Finally, the output voltage fluctuations are smoothed by the integrator, which is characterized by its integration time, τ. Commonly, a simple RC filter is used as an integrator.

The sensitivity of the radiometer is defined as the signal which will give a DC output voltage equal to the effective value of the output fluctuations due to the system noise [7.3]. When using an ideal integrator with integrating time τ, the sensitivity of a total power radiometer is given by (7.1) [7.1]-[7.4].

$$\Delta T = \frac{T_a + T_N}{\sqrt{B \cdot \tau}} = \frac{T_{sys}}{\sqrt{B \cdot \tau}} \tag{7.1}$$

Where T_a is the effective antenna noise temperature and B is the noise bandwidth of the receiver before the detector. For actual filter implementations the effective noise bandwidth is defined from the predetector power gain using (7.2) [7.1]-[7.3].

$$B = \frac{\left[\int_0^\infty G(f)df\right]^2}{\int_0^\infty G(f)^2 df} \tag{7.2}$$

The expression (7.1) accounts only for the measurement uncertainty due to noise fluctuations and does not incorporate receiver gain fluctuations. These gain fluctuations may however occur due to supply-voltage variations and to ambient temperature fluctuations. Then, the noise uncertainty and the gain uncertainty are caused by uncorrelated mechanism, hence they can be considered as statistically independent and the total rms uncertainty is given by (7.3) [7.1]-[7.3].

$$\Delta T = T_{sys}\sqrt{\frac{1}{B\cdot\tau}+\left(\frac{\Delta G}{G_0}\right)^2} \tag{7.3}$$

Where ΔG is the effective value of the receiver RF power gain variation, and G_0 is the average predetector power gain. In practice, $\Delta G/G_0$ is the determining term in (7.3) so that the actual sensitivity of the total power receiver is considerably less than the theoretical value. Therefore, total power operation is not suitable for high sensitivity radiometers [7.3].

7.1.2. The Dicke radiometer

The idea of using the modulation principle for eliminating fluctuations induced by receiver instabilities was introduced first by Dicke [7.5]. In this configuration, the radiometer input is switched between the antenna and a reference load at a modulation frequency, f_M. If f_M is high enough in comparison with the gain instability frequency then it is possible to detect the signal without gain fluctuations.

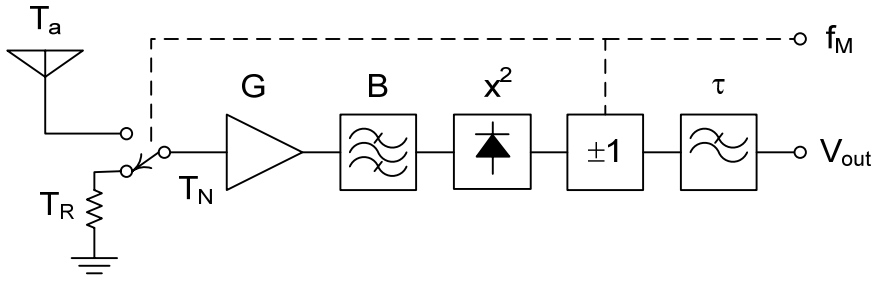

Fig. 7.2. Dicke radiometer.

At the ±1 multiplication stage output the voltage is independent of the receiver noise while the gain dependence is still present. Hence, the output uncertainty regarding the gain fluctuation can be expressed by (7.4).

$$\Delta T = (T_a - T_R)\frac{\Delta G}{G_0} \tag{7.4}$$

If the noise power from the antenna is equal to the noise power from the reference load the voltage fluctuations due to gain instability disappear and receiver sensitivity is determined by the system noise alone [7.3].

In this kind of radiometers the signal is connected to the receiver half of the time only degrading the sensitivity by a factor of $\sqrt{2}$. Moreover, the sensitivity is degraded by another factor of $\sqrt{2}$ due to subtraction of two noise signals. Therefore, the sensitivity of the Dicke receiver is given by (7.5) [7.4], which is half of the theoretical sensitivity of the total power radiometer.

$$\Delta T = 2\frac{T_{sys}}{\sqrt{B \cdot \tau}} \tag{7.5}$$

7.1.3. The correlation radiometer

In the correlation radiometer two or more receivers are connected in parallel and their signals are correlated in order to improve the overall sensitivity. In general two identical receivers are connected to orthogonal outputs of the same antenna, but there are other configurations that make use of the correlation between signals, e. g. the receivers can be connected to different antennas resulting in an interferometer with correlation receiver [7.2].

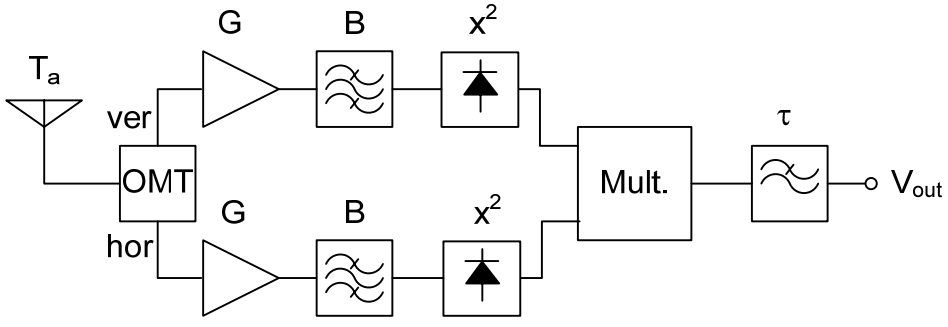

Fig. 7.3. Correlation radiometer.

The multiplier output contains only a correlation signal proportional to the incoming antenna noise power which is the same for both receivers. The noise powers from the receivers are uncorrelated and, hence, they are not present in the output. The sensitivity of the correlation receiver is given by (7.6) [7.3].

$$\Delta T = \sqrt{2}\frac{T_{sys}}{\sqrt{B\cdot\tau}}\sqrt{1+\left(\frac{0.5T_a}{T_{sys}}\right)^2} \tag{7.6}$$

Where T_{sys} is the addition of the receiver noise temperature and half of the antenna noise temperature. If the antenna noise is small in comparison with receiver noise then the sensitivity, given by (7.7), is improved by a factor of $\sqrt{2}$ regarding the Dicke radiometer. Hence, the correlation radiometer is useful only when the antenna noise is small.

$$\Delta T = \sqrt{2}\frac{T_{sys}}{\sqrt{B\cdot\tau}} \tag{7.7}$$

7.1.4. The pseudo-correlation radiometer

This kind of radiometer is an evolution of the receiver presented in the previous section and it is included here because it is used for the low frequency instruments of the PLANCK[2] space mission, which is the seed of this thesis.

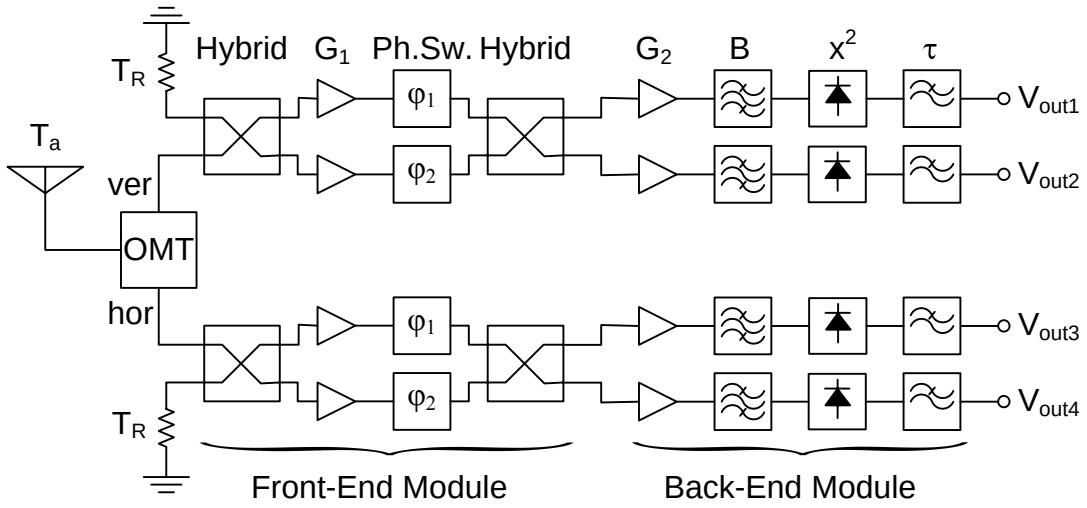

Fig. 7.4. Radiometer block diagram of the PLANCK low frequency instruments based in a pseudo-correlation scheme.

The pseudo-correlation radiometer combines the comparison with a reference load from the Dicke radiometer with the combination of signals from the correlation radiometer. This configuration improves the classical Dicke scheme avoiding the presence of an active switch in the receiver front-end and increasing the sensitivity by a factor of $\sqrt{2}$. In this design the antenna temperature is continuously compared to the stable reference load to reduce the effect of instabilities in the front-end amplifiers, while a fast switching between the two signals using phase switches provides immunity

[2] PLANCK is an European space observatory whose main goal is to measure tiny fluctuations in the CMB with improved accuracy over previous projects like COBE and WMAP from NASA.

to back-end fluctuations [7.6], [7.7]. Therefore, the sensitivity of the pseudo-correlation radiometer can also be expressed with (7.7), where T_{sys} is the addition of the antenna noise temperature and the noise temperature of one receiver branch.

7.1.5. The polarimetric radiometer

The polarimetric radiometer is another variation of the correlation radiometer and it is included here because it is used for the QUIJOTE project, which will be explained in more detail in the following sections. The polarimetric radiometers are used to find the so-called Stokes parameters which enable to determine the polarization state of an electromagnetic radiation.

The first and second Stokes parameters, I and Q, are measured conventionally using vertical and horizontal polarized radiometer channels, followed by addition or subtraction of the measured antenna temperatures. The third Stokes parameter, U, can be measured with a conventional two-channel radiometer connected to an orthogonally polarized antenna rotated 45º with respect to the vertical and horizontal directions, and subtracting the measured antenna temperatures. Finally, the fourth Stokes parameter, V, can be measured with the two-channel radiometer connected to a left-hand/right-hand circularly polarized antenna system [7.4], [7.8]. For the QUIJOTE project the Stokes parameter V is not measured since it is assumed that the CMB has not circular polarization.

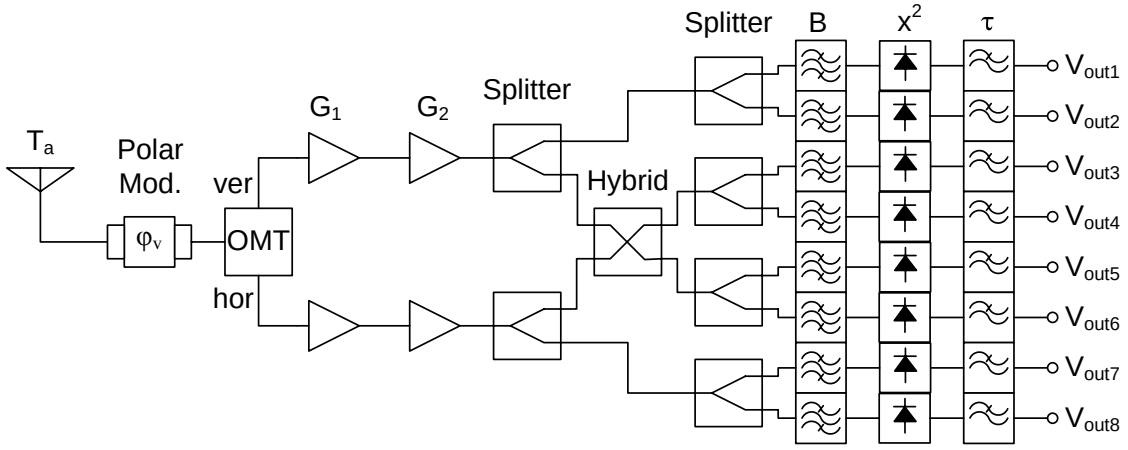

Fig. 7.5. Radiometer block diagram of the QUIJOTE project for the 10 – 14 GHz and 16 – 20 GHz bands. Each band is sub-divided into two subbands at the filter stage.

In Fig. 7.5 a block diagram of the polarimeter radiometer used for the lower bands of the QUIJOTE project is presented. The higher band, 26 – 36 GHz, employs a simplified scheme which will be discussed in next section.

The key component in the radiometer of Fig. 7.5 is the polar modulator placed before the orthomode transducer (OMT). The polar modulator rotates at a frequency f_M

providing a rotating reference system for the vertical and horizontal components in the OMT. Thus, the orthogonal components of the antenna signal can be obtained both in the reference system with 0º and with 45º, enabling the measurement of Stokes parameters I, Q and U simultaneously. In this configuration the angular positions are repeated four times per turn, therefore the polar cycle is four times the rotation frequency.

If the modulator rotation frequency is high enough then the polar cycle is faster than the low frequency gain fluctuations and hence its effect is eliminated from the output signal. In this case the instantaneous sensitivity of each individual Stokes parameter can be calculated using (7.7).

7.2. The QUIJOTE Project

The standard theory of the Big-Bang predicts that the CMB is linearly polarized. The physical mechanism responsible for its polarization is the Thomson scattering during the recombination or reionization epochs [7.9].

The QUIJOTE (Q-U-I JOint TEnerife) CMB experiment is a project to be installed and operated in the Teide observatory (Canary Islands, Spain) aimed for characterizing the polarization of the CMB, and other galactic and extragalactic physical processes in the frequency range 10 – 30 GHz.

The project has two phases. Phase I, which is now under development, consists in the construction of a first telescope and two instruments which can be exchanged in the focal plane. The first instrument is a multichannel instrument providing the frequency coverage between 10 and 20 GHz, plus a single pixel at 30 GHz. The second instrument will consist of 16 polarimeters working at 30 GHz. The temperature sensitivity per beam is calculated using (7.8) [7.9].

$$\Delta Q = \Delta U = \sqrt{2}\frac{T_{sys}}{\sqrt{B \cdot \tau \cdot N_{ch}}} \tag{7.8}$$

Where N_{ch} is the number of channels. Phase I also includes a source subtractor facility to monitor and correct the contribution of polarized radio-sources in the final maps. Phase II, not funded yet at the moment of finishing this thesis, considers the construction of a second telescope identical to the first one and a third instrument with 30 polarimeters at 40 GHz.

(a) (b)

Fig. 7.6. (a) Artist view of the two telescopes installed in their enclosure; (b) The first telescope for installing the first and second instruments.

7.2.1. QUIJOTE first instrument description

The QUIJOTE first instrument is a multi-frequency receiver with five separate polarimeters. Figure 7.7 shows an artist view of the instrument. The sky radiation is captured by five conical corrugated feedhorns, two of which operate in the frequency band 10 – 14 GHz, other two at 16 – 20 GHz, while the central horn operates at 26 – 36 GHz.

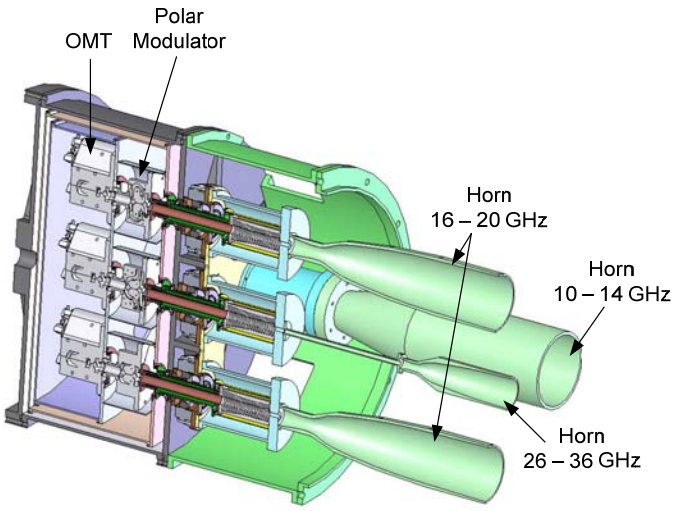

Fig. 7.7. Cross section of the QUIJOTE first instrument.

Figure 7.5 shows the block diagram of the lower frequency bands radiometers. In the cryostat, cooled down to 20 K, there are the horn throat, input waveguides, polar modulator, OMT, and first RF amplification stage. The polar modulator produces the modulation of the light polarization and spins at a programmable frequency in the 10 – 40 Hz range. The signal then passes through the OMT, which provides the two orthogonal linear polarizations that are later amplified in the low noise cryogenic

amplifiers. These two orthogonal signals are fed into a room temperature back-end module (BEM). Here the signals are further amplified, separated in successive power splitters and spectrally filtered in such a way that the initial band is separated into four lower-side band channels and other four upper-side band channels, each with 2 GHz bandwidth. Each signal is detected by a square-law detector and recorded for post-processing.

The receiving system of the central radiometer at 26 – 36 GHz is a slightly different version. It lacks power splitters and hence there are only two output channels corresponding to the two orthogonal polarizations. The block diagram of this radiometer is presented in Fig. 7.8.

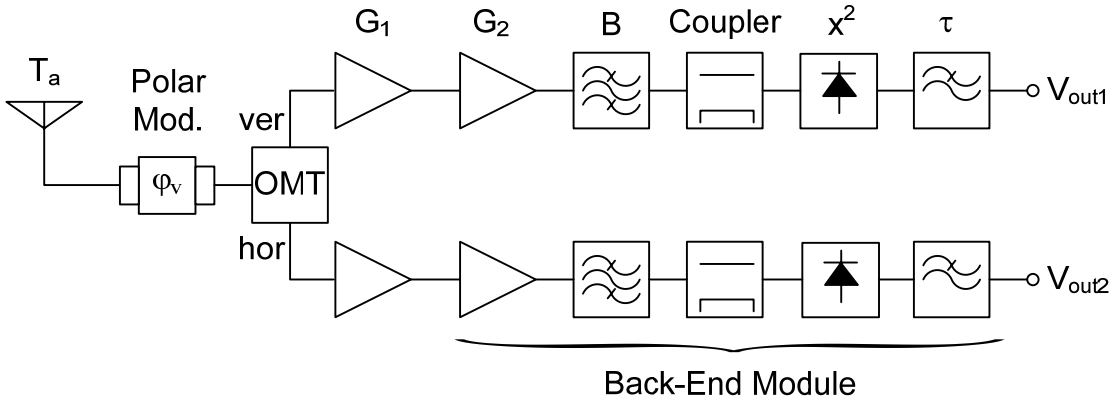

Fig. 7.8. Block diagram of the 26 – 36 GHz radiometer.

In the following, some subsystems of the QUIJOTE radiometers, in which the DICOM has actively participated, are detailed: the polar modulators for all bands, which are an original design from R. Hoyland (Instituto de Astrofísica de Canarias, Tenerife, Spain), the OMTs, which have been designed at the DICOM, and finally, the 26 – 36 GHz BEMs which have been completely designed and assembled at the DICOM.

7.2.2. QUIJOTE polar modulators

Earlier designs of polar modulator have included rotating grids held at 1/4λ over reflecting plates such as in the COFE/B-machine [7.10]. This leads to a complicated optical arrangement and has until recently been narrow band (< 20%). Recent designs of dielectric half-wave plates [7.11] which are transmission rather than reflection based have produced very low loss and wide band designs.

The polar modulator designed for QUIJOTE is novel in the fact that it is made from waveguide components. The advantage of this is that it can be made smaller than a grid or dielectric modulator and thus can be spun faster and therefore can be used in radiometers that suffer significant 1/f noise. It is also inserted into the radiometer circuit

after the feedhorn. This means that effectively the feedhorn defines the level of cross-polarization of the optical assembly rather than the modulator.

The polar modulator is based on the turnstile junction design presented in Section 7.2.3. An incoming signal is split equally into four rectangular waveguides by the turnstile junction. Each orthogonal waveguide pair is sent through a path with 180º difference to the other. A broadband 180º path difference is achieved through equal and opposite E-plane bends and simple waveguide-coaxial-waveguide transitions resulting in a symmetrical and asymmetrical configuration. Finally the four waveguides are brought together again into a second turnstile junction similar to the first.

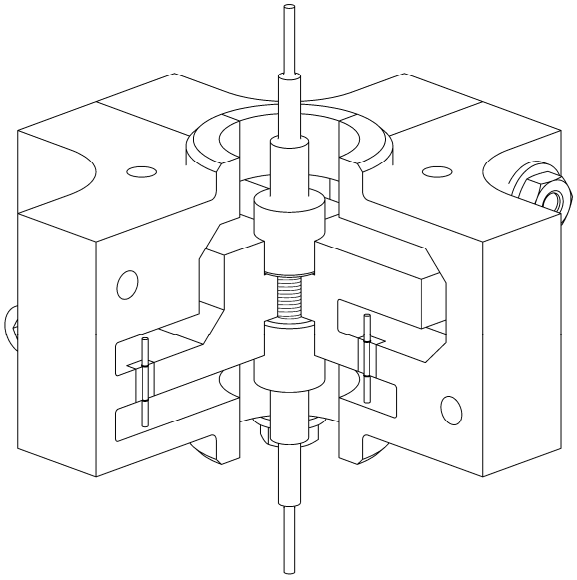

Fig. 7.9. Internal view of the polar modulator showing coaxial probes and turnstile junctions.

Figure 7.9 shows the designed polar modulator with one quarter removed. The four-stage scatterer of the two orthomode junctions can be seen to protrude out from the circular waveguide input and output. Two orthogonal reduced height waveguide paths can be seen in either face of the cut-away. The polar modulator is conveniently made from four separate quadrants which are joined along the E-plane of each rectangular waveguide. In the lower half of each face a centre pin and dielectric can be seen adjoining top and bottom waveguide paths.

In Fig. 7.10 the two orthogonal branches are presented showing the relative phase of mode TE_{10} at given points in the rectangular waveguides. From Fig. 7.10, it is clear from the geometry of waveguide bends in the top waveguide section that anti-phase signals result at the coaxial interfaces.

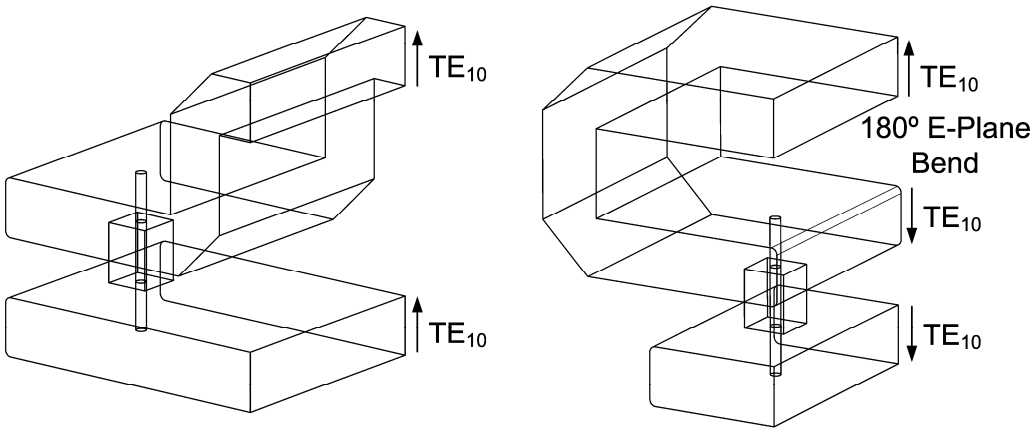

Fig. 7.10. Polar modulator branches; (a) with symmetric waveguide-waveguide connection; (b) with asymmetric waveguide-waveguide connection. Electrical length of both branches is identical.

The waveguide-to-waveguide transition is accomplished using E-plane antenna probes. A central conductor is designed to reach into both waveguides whereas the dielectric is accommodated in the modulator structure. For the 10 – 15 GHz band (WR75), the central conductor is designed with diameter d = 0.82 mm. The length and location of the probes are optimized for a broadband performance, in this case, 3.9 mm long probes placed at 5.65 mm from the waveguide short circuit.

For the measurement of the polar modulators available orthomode transducers (see Section 7.2.3) were used as adapters to the circular waveguide input and output. The unused rectangular port of each OMT was terminated with commercially available rectangular waveguide terminations. TRL calibration was carried out at the OMT circular waveguide ports using purpose-built calibration shorts and 1/4 wavelength circular waveguide sections. Purpose built adapters were used to convert the four bolt interface of the polar modulators to adapters with eight alignment holes equi-spaced (every 45º) about the waveguide axis. This allowed rotation of the modulator and orthomode transducer necessary to perform all the measurements, i.e. 0º, 45º, 90º, etc.

Figure 7.11 shows the polar modulator return loss both simulated (a) and measured (b) for three polar modulator angles: 0º, 45º and 90º. Further rotation of the modulator is degenerate since a 180º rotation provides the same measurement as 0º. Both simulation and measured data show return losses < -20 dB across the whole 10 – 15 GHz band and generally better than -25dB apart from a few peeks that appear in the measured data.

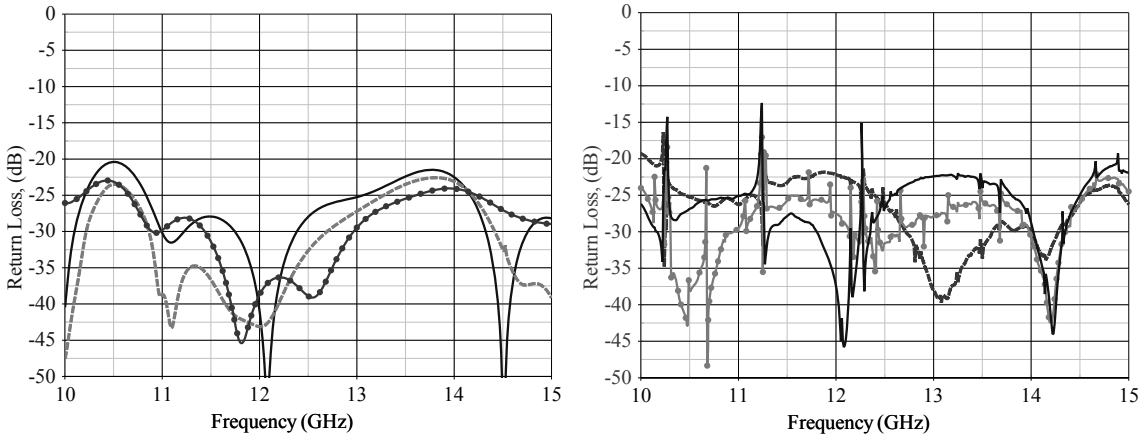

Fig. 7.11. Return Loss simulations (a) and measurements (b) of mode TE_{11} at input for 3 polar modulator orientations ; 0º(solid), 45º(dashed) and 90º(circle) with respect to the E-plane split along one of the rectangular waveguides.

The peeks appearing in all measurement results have been investigated both experimentally and through simulation. It can be seen that the axial alignment is the cause of these in-band peeks and that the test set used here does not provide sufficient alignment precision to fully characterize these components. A simple simulation of several radial offset cylindrical sections in series shows that a misalignment of only ±100 μm is enough to cause the level of spikes that can be seen in the band.

Figure 7.12 shows the corresponding insertion loss simulations and measurements for each of the polar modulator orientations 0º, 45º and 90º. Note that for the 45º orientation the output is measured through the orthogonal polarization due to the action of the modulator. It can be seen that the insertion loss is generally flat across the whole band 10 – 15 GHz and < -0.15 dB in the measured data (no account is taken of resistive loss in the simulation).

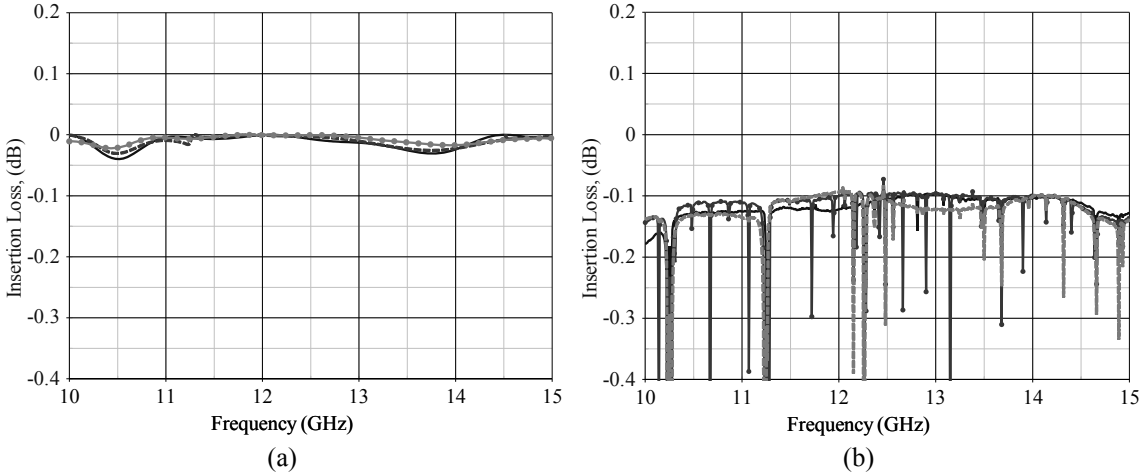

Fig. 7.12. Insertion Loss simulations (a) and measurements (b) of mode TE_{11} at input for three polar modulator orientations ; 0º(solid), 45º(dashed) and 90º(circle) with respect to the E-plane split along one of the rectangular waveguides.

Figure 7.13 shows the simulated and measured phase difference between the S_{21} measurements of the two different routing arms in the polar modulator. The simulations and measurements show a difference of 180 ± 2º apart from several peeks that appear in the measured data. The simulated and measured results are very similar.

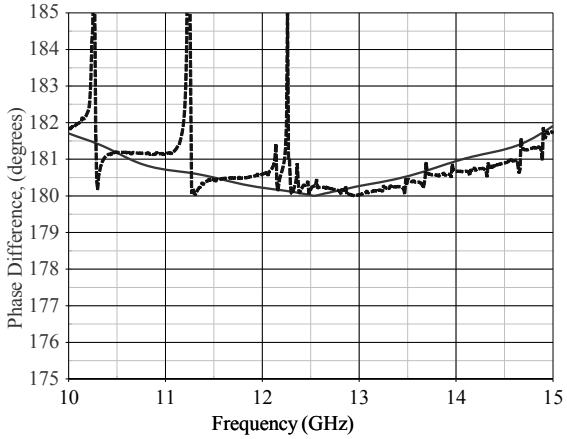

Fig. 7.13. Simulated (solid) and measured (dashed) results of the phase difference between both TE_{11} polarizations through the polar modulator.

Figure 7.14 shows the simulated (a) and measured (b) polar isolation between 0ºand 90º (solid) and 45º and 135º (dashed). The measured 0º isolation is better than -30 dB and generally better than -40 dB across the whole 10 – 15 GHz band whereas simulated data predicts < -50 dB isolation. The measured 45º isolation is better than -15 dB and generally better than -20 dB across the whole 10 – 15 GHz band whereas simulated data predicts < -25 dB polar isolation.

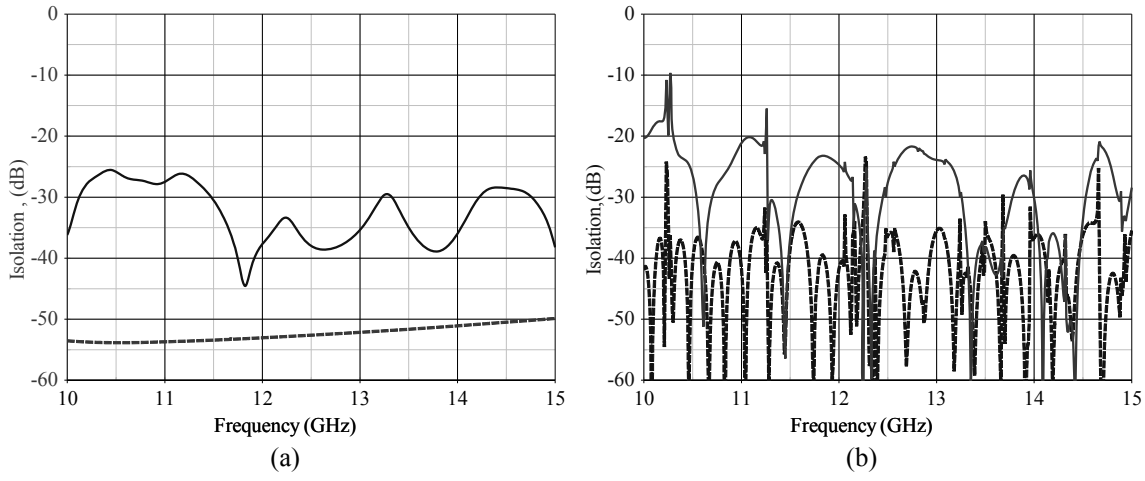

Fig. 7.14. Simulated (a) and measured (b) polar isolation between 0ºand 90º (solid) and 45º and 135º (dashed) polar modulator orientation.

The polar modulator has been successfully scaled to the WR51 band and the WR28 band. Figure 7.15 shows a photo of the three modulators, one for each of the bands. All mechanical parts have been scaled in such a way that they can be machined

on standard workshop numerically controlled lathes and milling machines apart from the coaxial parts which were all machined on the LPKF[3] micro-milling machine.

The WR51 polar modulator presents a return loss < -19 dB, insertion loss < 0.3 dB, and polar isolation < -30 dB measured at 0º and 45º references. The WR28 polar modulator shows a return loss < -17 dB, insertion loss < 0.6 dB, polar isolation < -17 dB measured at 45º reference and polar isolation < -22 dB measured at 0º reference.

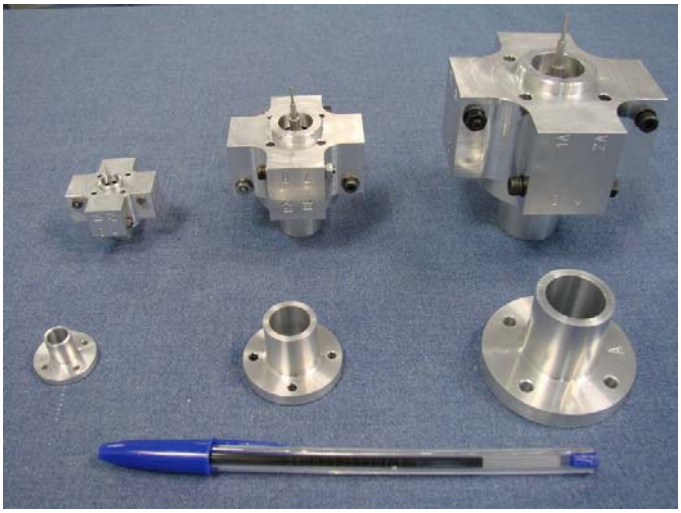

Fig. 7.15. The polar modulators prior to surface treatment (from left to right) WR28 band, WR51 band and WR75 band. The modulators are surface treated with a coating of Alodine 1200 on its conducting surfaces whilst on its outer surfaces they are anodized for mechanical protection. The outer surface is black to aid radiative cooling.

7.2.3. QUIJOTE orthomode transducers

The OMT is a key component in the polarimeter since it separates linear orthogonal polar components and therefore sets a limit on the cross-polarization. Several structures have been proposed in the literature over the last years [7.12]-[7.18].

The OMT designed for this project is based on the turnstile junction. The scatterer used in the turnstile junction is designed as a four-step cylindrical structure. It is machined separately and then screwed on to the OMT body to obtain a good electrical contact. It is a single unit which can be easily interchanged to provide bandwidth tuning. Single mitered E-plane bends and single-step power dividers in reduced height waveguides (a = 4b) are used in this OMT to improve bandwidth, phase equality and return losses by carefully avoiding high order mode propagation. To achieve phase matched outputs special care has been taken during mechanical design to maintain symmetry in both arms of the structure as well as to provide outputs in the same physical plane to help the receiver design. The designed OMT makes the above improvements to the classical turnstile junction orthomode transducer thus providing

[3] LPKF Laser & Electronics AG, D-30827 Garbsen, Germany.

low-cost, easier manufacture, wideband and improved electromagnetic performance over other OMTs in the same bands for phase-balanced operation. This simplified mechanical design allows a straightforward frequency scaling to other waveguide bands.

The internal view of the orthomode transducer is presented in Fig. 7.16. The circular waveguide input can be seen as well as the two orthogonal rectangular waveguide outputs. The rectangular waveguide outputs lie in the same plane but they have been offset from the circular axis to avoid waveguide overlapping. A series of E-plane bends, seven on each arm, and two single-step power dividers provide critical phase equal paths through each of the four arms that excite the turnstile junction.

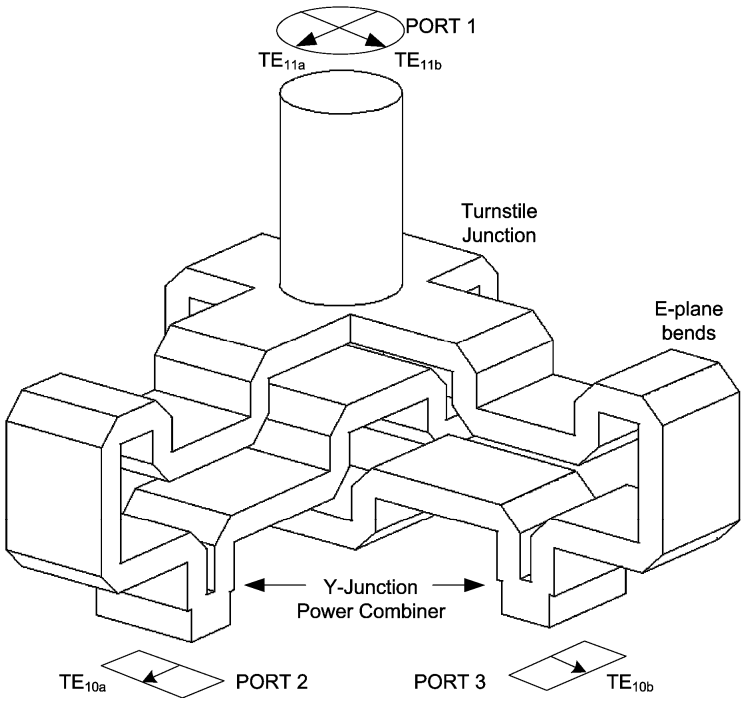

Fig. 7.16. Internal view of the designed orthomode transducer with the port definition as modeled in the 3D electromagnetic simulator HFSS.

The role of the turnstile junction is to split the incoming electromagnetic wave into orthogonal polarizations. Therefore mode TE_{11} at port 1 (see Fig. 7.16) will be separated into two orthogonal signals, TE_{11a} and TE_{11b}, having the same cutoff frequency. A scatterer placed at the junction base along the circular waveguide axis separates these components according to their polarization. TE_{11a} is split equally and in anti-phase between both branches of the arms leading to port 2, and is not propagated through the arms associated with port 3. It is then combined again in the Y-junction of port 2. The same argument applies to TE_{11b} and port 3. The turnstile junction shown in Fig. 7.17 has been simulated and the S_{11} (dB) results are plotted in Figure 7.18.

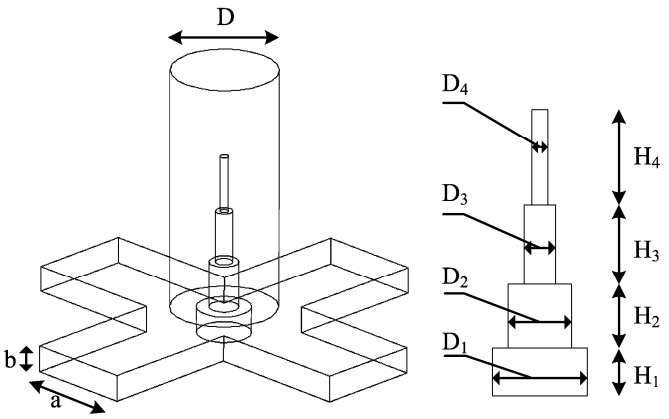

Fig. 7.17. Simulated turnstile junction structure. Dimensions can be found in Table 7.1.

The scatterer acts as a tuning stub enabling selection of the working bandwidth without changing the orthomode transducer structure. Therefore, the bandwidth can be shifted or modified by simply changing the scatterer. Figure 7.18 shows simulation results of the same turnstile junction in which the bandwidth has been narrowed by modifying the number of cylindrical sections in the scatterer and their diameters. These new dimensions can be found in the last column of Table 7.1.

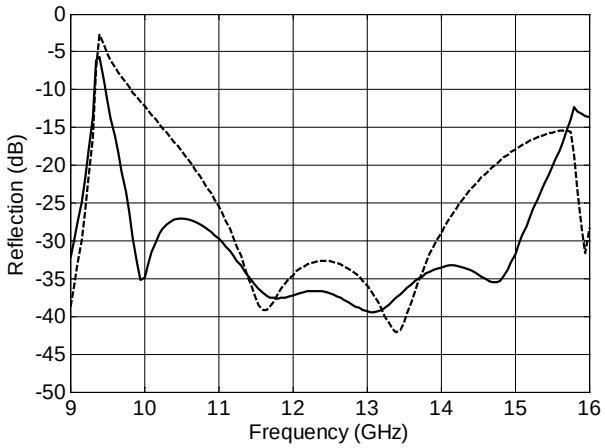

Fig. 7.18. Simulated reflection S11 (dB) of the designed wideband turnstile junction is plotted in solid line; result of the same structure with the scatterer exchanged to get a narrowband design is plotted in dashed line.

Parameter	Wideband design (mm)	Narrowband design (mm)
D	19	19
a	19	19
b	4.75	4.75
H_1	4.75	5.36
H_2	8.5	8.87
H_3	9.4	-
H_4	10.15	-
D_1	9.6	8.64
D_2	5.2	3.63
D_3	3	-
D_4	1.45	-

Table 7.1. Turnstile junction dimensions.

The OMT is completely designed using single mitered E-plane bends and reduced height waveguides. The main advantage of this strategy is to increase the usable bandwidth. The bandwidth is limited at the lower end by the cutoff frequency of the fundamental propagating mode, TE_{10} in the rectangular waveguide or TE_{11} in the circular one, and at the higher end by the cutoff frequency of higher order modes. An E-plane bend excites the spurious higher order mode TM_{11} whereas in an H-plane bend the mode TE_{20} is excited [7.19]. In standard waveguide the degenerated modes TM_{11}/TE_{11} have a higher cutoff frequency than the TE_{20} mode.

Power combination is carried out by using single stepped E-plane Y-junctions. Another advantage of the use of reduced height waveguides is that they give good results with very simple and compact structures. The Y-junction proposed for this OMT needs only one step matching compared with more complex designs using standard waveguide proposed in the literature [7.16], [7.17].

For the mechanization, the OMT body is divided into four pieces which join along the circular waveguide axis and consequently split the rectangular waveguides at their E-field mid-plane. This gives minimum resistive losses in the waveguides and allows the use of standard mechanical machining techniques to be used. Each piece is physically different, the largest of which is shown in Fig. 7.19. Aluminum 6061 was chosen as the body material for its availability, excellent mechanical properties and ease of surface treatment. For this application a surface treatment of Alodine 1200 was chosen to maintain high conductivity throughout its working life. Alternatively the surface could be gold-plated.

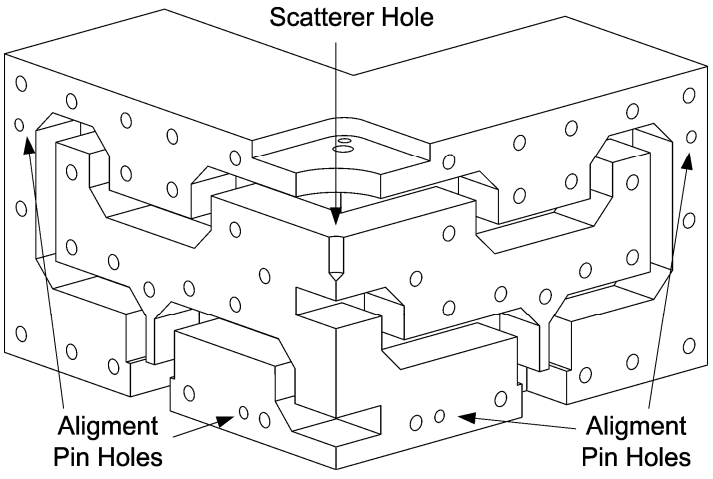

Fig. 7.19. Internal faces of one orthomode transducer quarter. The scatterer hole thread is made at the final step with all the parts assembled.

A critical part of the turnstile junction is the scatterer. A good electrical contact between the scatterer base and the four OMT quarters is essential. To achieve this, this component is machined with a thread in its base (see Fig. 7.20) so it can be screwed into

the scatterer hole of Fig. 7.19. Moreover, a chamfer is made in the base to assure a good electrical contact at the cylinder perimeter avoiding problems that occur if the base flatness is poor. Practically this was found to be insufficient and resulted in higher insertion loss and lower cross-polar isolation. A small amount of conductive epoxy or silver paint can be applied to the base of the scatterer to improve the contact and thus the insertion loss and isolation.

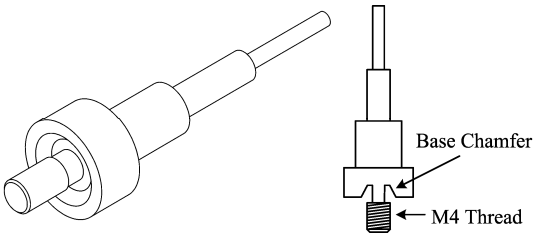

Fig. 7.20. Detailed view of the designed scatterer. A base chamfer assures good electrical continuity with turnstile base in case of poor flatness in the scatterer base.

Measurement results for the WR75 OMT are shown in the following. Port matching at the rectangular ports is plotted in Fig. 7.21a while isolation between rectangular ports is shown in Fig. 7.21b. The differences between simulation and measurement setups (for measurements two OMTs are connected through their circular ports and then measured; for simulation only one OMT is defined connected to perfect matched ports) produce the discrepancies between simulations and measurements in the following figures. Also misalignment of the circular waveguide adapters can be shown to be a source of spikes in the measurement data. Insufficient alignment precision was provided for such a fine measurement as this, since misalignment of >100 μm are enough to produce spikes at this level.

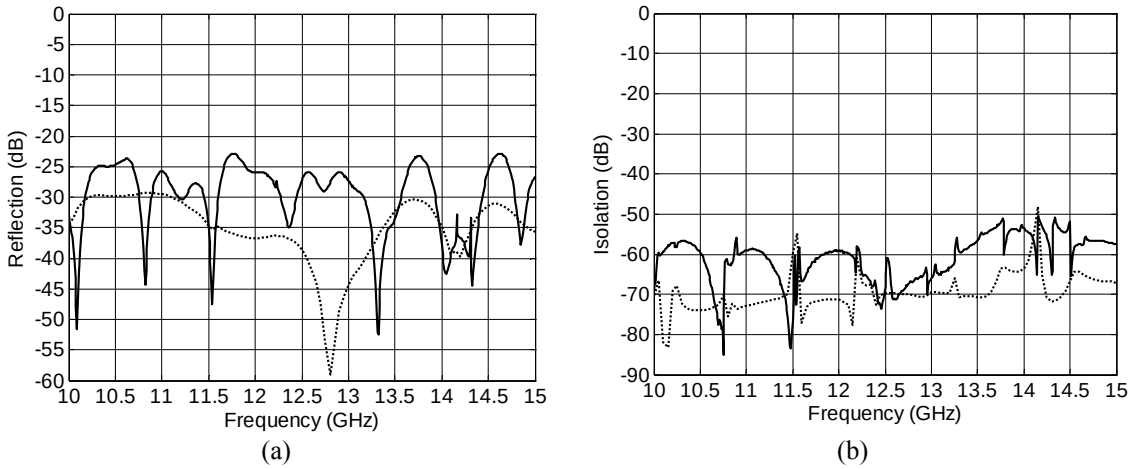

Fig. 7.21. (a) Reflection, S11 (dB), results at the rectangular port for the designed orthomode transducer: measurement in solid line and simulation in dashed line; (b) Isolation results between rectangular ports for the orthomode transducer: measurement in solid line and simulation in dashed line. Cross-polarization isolation, which is measured between rectangular-circular ports, is more important to the QUIJOTE experiment and is normally better than these values.

Reflection measurements show >23 dB return loss in the band and are very similar for both rectangular ports, therefore only one curve is plotted for clarity. The isolation between rectangular ports is very good with values of 55 dB in the band. Results of transmission and phase difference are shown in Fig. 7.22a and Figure 7.22b respectively. An insertion loss around 0.05 dB is measured in both arms in the whole band. The maximum phase error between arms is 0.7º across the WR-75 band, which is an excellent result for applications where phase matched outputs are required.

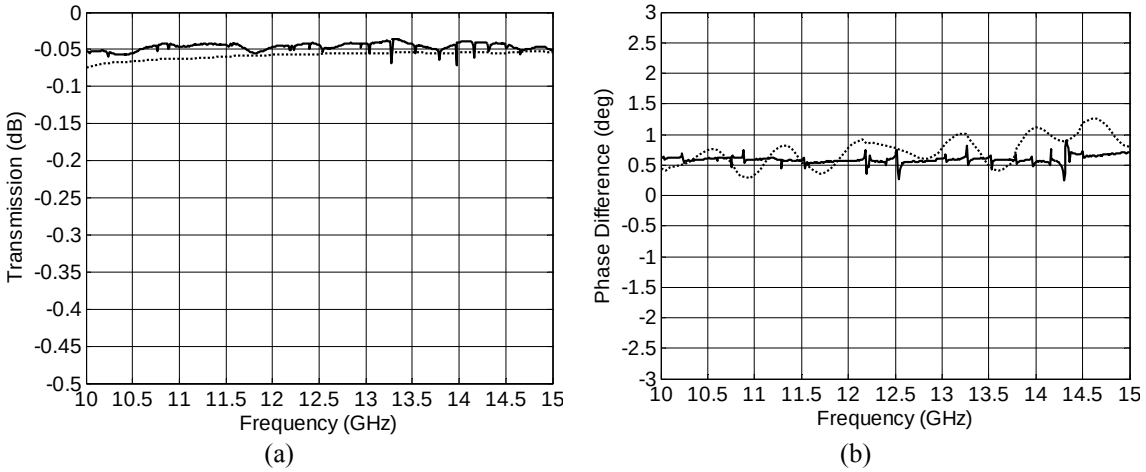

Fig. 7.22. (a) Insertion loss, S21 (dB), results for one arm of the designed orthomode transducer: measurement in solid line and simulation in dashed line; (b) Phase difference results between orthomode transducer arms: measurement in solid line and simulation in dashed line.

All the dimensions are electrically scaled to the WR51 and WR28 waveguide bands keeping the same configuration for all OMTs as can be seen in Fig. 7.23.

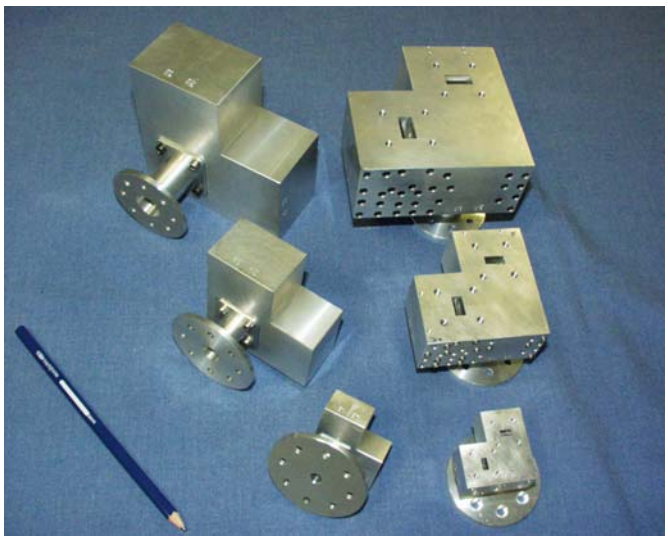

Fig. 7.23. Picture of the WR75, WR51 and WR28 orthomode transducers for the QUIJOTE cosmic microwave background experiment.

The return loss of the WR51 OMT is better than 20 dB and the isolation better than 45 dB, while the insertion loss is around 0.1 dB. For the WR28 dB, the return loss

is around 20 dB with isolation around 40 dB and an insertion loss of 0.2 dB. The phase differences between arms are less than 1º and 2º respectively for the WR51 and WR28 bands which make these OMTs suitable for applications where phase matched outputs are critical.

7.2.4. QUIJOTE 26 – 36 GHz back-end module

The 26 – 36 GHz BEM follows the block diagram presented in Fig. 7.8 and it is designed according with the preliminary specifications of Table 7.2. The two branches are separated in two identical modules which are detailed in the following.

Parameter	Value
Bandwidth	26 – 36 GHz
Input Power	-53 dBm (expected from FEM)
Output DC voltage (before video Amp)	in the range 1 – 10 mV
Input Interface	WR28 Flange
Output Interface	RF Output: 2.92 mm connector DC Output: detected voltage
Noise (T_e)	< 500 K

Table 7.2. QUIJOTE preliminary 26 – 36 GHz BEM specifications.

The first element in the BEM RF chain is a transition to couple the incoming energy from the input WR28 waveguide to the microstrip line needed for the low noise amplifiers. The transition, designed on Alumina substrate (ε_r = 9.9, h = 10 mils), is based on [7.20]-[7.22]. Figure 7.24 shows the artist view of the RF elements assembly in the BEM module.

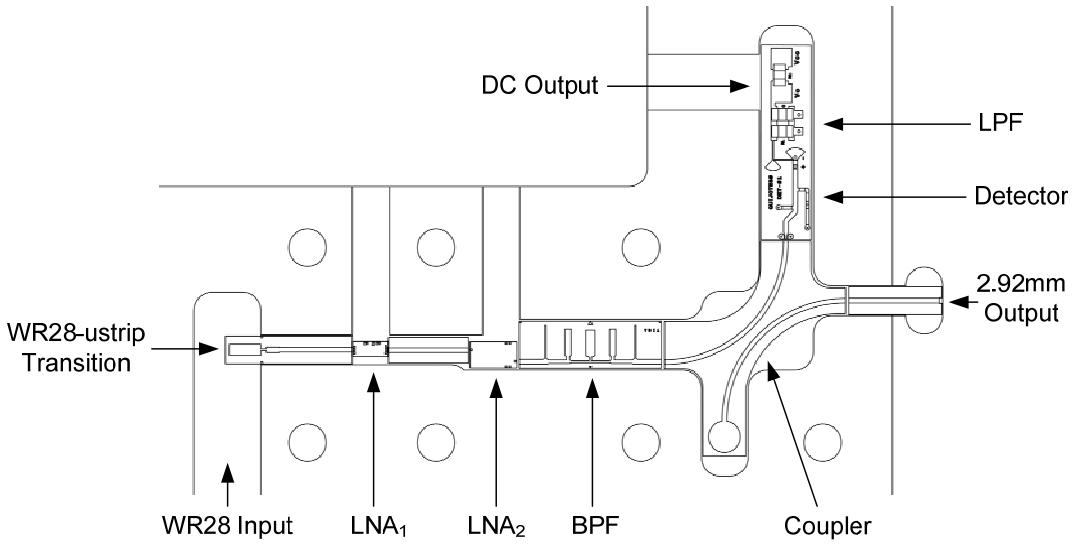

Fig. 7.24. Artist view of the assembly showing the RF elements in the BEM module.

The gain of the radiometer is accomplished using commercially available low noise amplifiers since they can fulfill the project requirements, thus speeding up the development process. Because of the high gain needed for the BEM (around 30 dB) two low noise amplifiers are used. The first one is model AMMC6241 from Avago

Technolgies[4] which offers low noise with high associated gain; whereas the model ALH140 from NGST[5] is used for the second amplifier since it provides medium gain with good matching and a higher compression point.

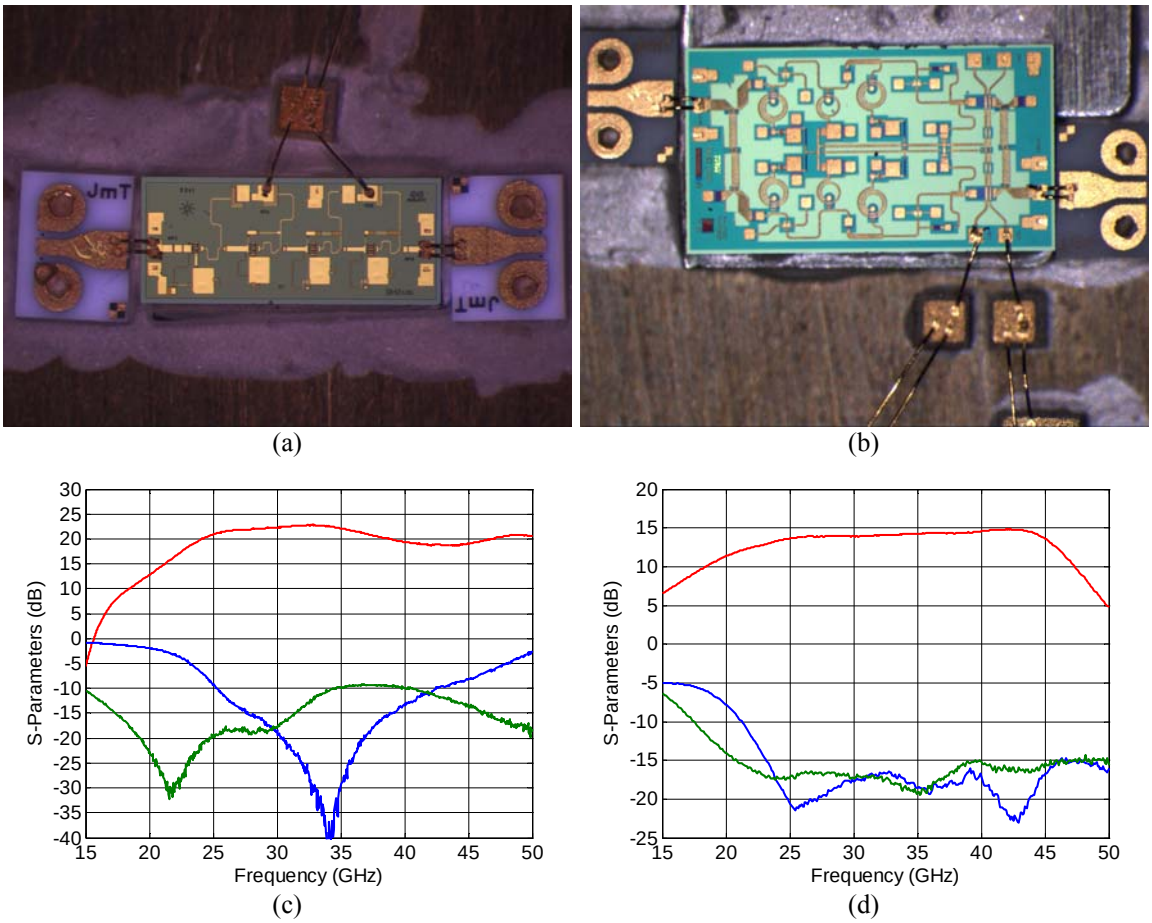

Fig. 7.25. Low noise amplifiers measurement using coplanar-to-microstrip transitions from Jmicro[6]; (a) AMMC6241; (b) ALH140; (c) results from AMMC6241 with nominal bias settings: Vd = 3V, Id = 62mA; (d) results from ALH140 with nominal bias settings: Vd = 4V, Id = 60mA. Gain is shown in red, input matching in blue, and output matching in green.

The band pass filter is designed on Alumina substrate (ε_r = 9.9, h = 10 mils). It is based on a stub filter to fulfill bandwidth requirements, which are difficult to achieve with a coupled line filter. Figure 7.26 shows a picture of the filter during its characterization with coplanar-to-microstrip transitions (ProbePoint™ 1003 from Jmicro) for on-wafer measurements.

[4] Avago Technologies, 95131, San Jose, CA, USA.

[5] Northrop Gumman, 90067-2199, Los Angeles, CA, USA.

[6] Jmicro Technology, Inc., 97229, Portland, OR, USA.

(a)

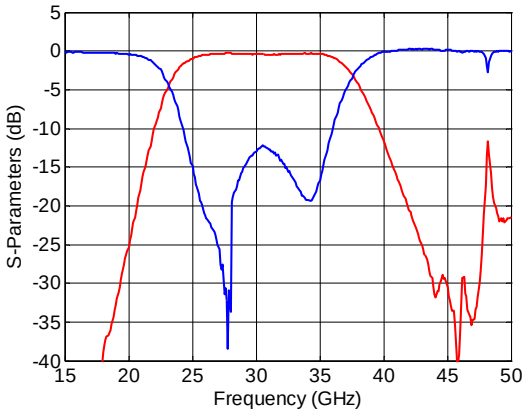

(b)

Fig. 7.26. Band pass filter characterization; (a) picture of the designed filter, dimensions 7.6x2.5 mm^2; (b) measurement results: insertion loss (red) maximum 0.8 dB, and return loss (blue) better than 10 dB.

The directional coupler is used in the BEM to extract a sample of the RF signal before the conversion to DC voltage, thus enabling BEM RF characterization and tuning if needed. Hence, the coupling factor is low, which facilitates the broadband design.

The designed coupler follows the proposed structure given in [7.23]. The coupler is designed with a target coupling factor of 13 dB on the same substrate as the other planar elements within the BEM. The 50 Ω dot-termination is achieved using the 20 Ω/□ NiCr resistive layer of the Alumina substrate. Coupler picture during characterization and its results are shown in Fig. 7.27. The maximum insertion loss is 0.6 dB in the band, whereas the coupling is 13.2 dB ± 0.9 dB.

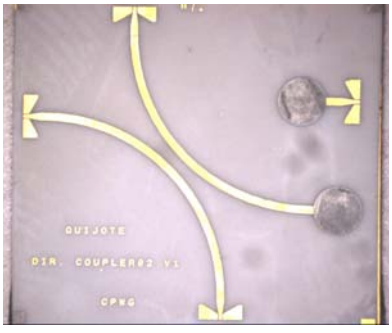

(a)

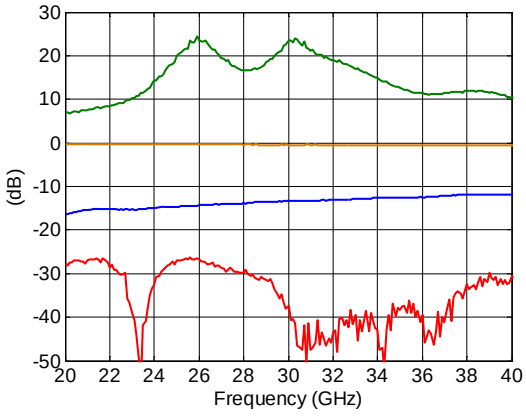

(b)

Fig. 7.27. Designed directional coupler for the 26 – 36 GHz BEM; (a) picture during measurements; (b) coupler performance: return loss (red), coupling (blue), directivity (green), and insertion loss (orange).

Finally, the detector converts the signal from RF power to DC voltage. For this purpose it is designed a square-law detector using the zero-bias beam lead Schottky diode model MZBD-9161[7]. The input matching network is designed using thin film resistors, taking advantage of the Alumina resistive layer, to flatten the frequency response.

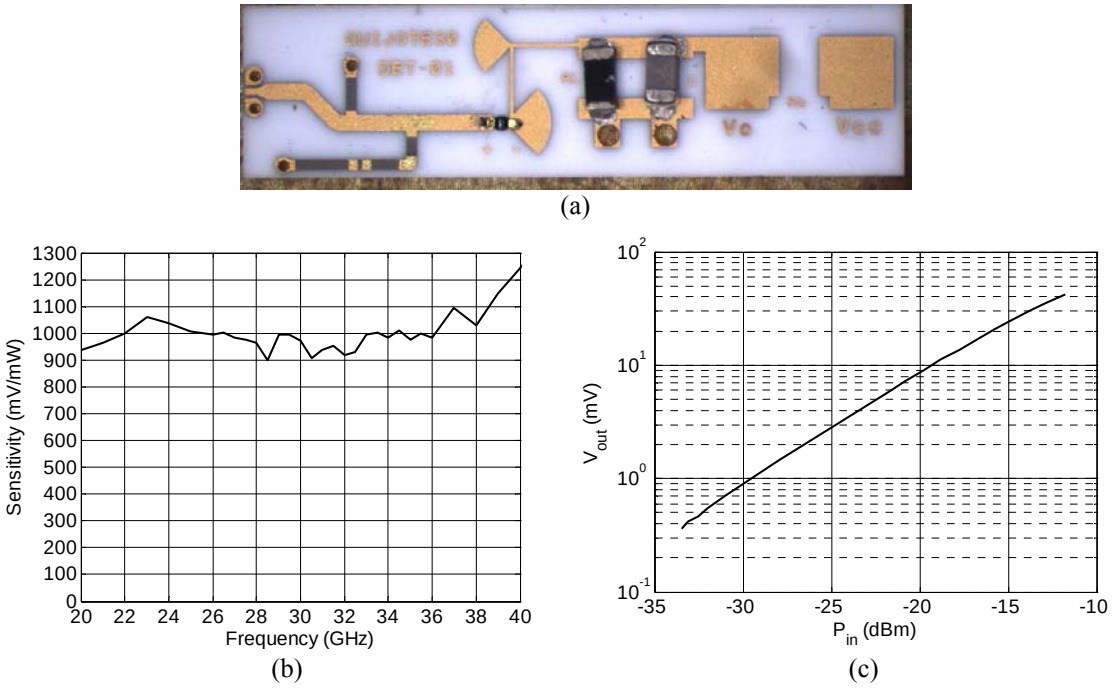

(a) (b) (c)

Fig. 7.28. Designed detector with the RC low pass filter included; (a) detector picture; (b) detector sensitivity with P_{in} = -30 dBm; (c) detector compression at f_{in} = 31 GHz. P_{1dB} = 13.8 dBm.

The detected voltage needs to be amplified in order to reach suitable levels for the analog-to-digital converters used in the data processing. This amplification is carried out with a video amplifier which provides high gain as well as balanced outputs. The scheme of this video amplifier is shown in Fig. 7.29.

[7] Aeroflex Metelics, 03053, Londonderry, NH, USA.

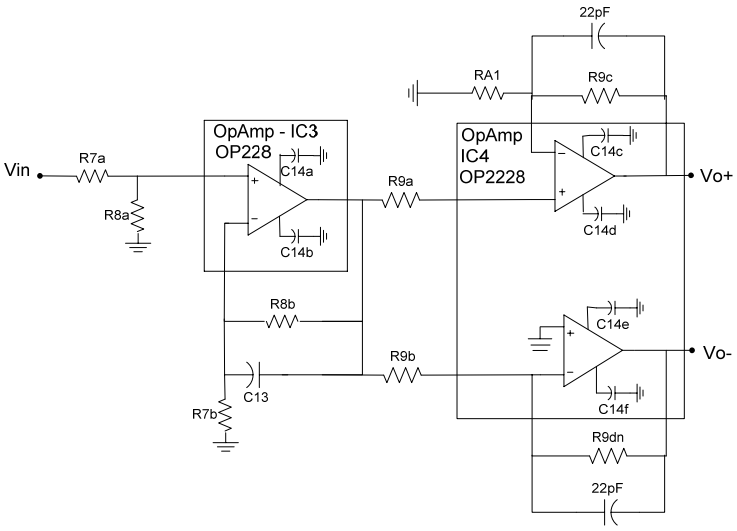

Fig. 7.29. Video amplifier scheme.

The BEM is biased using only a 5 V power supply, therefore suitable DC subcircuits need to be included in the DC printed circuit board (PCB) to generate adequate voltage levels to bias all the subcircuits within the BEM. Figure 7.30 presents a block diagram of the DC PCB.

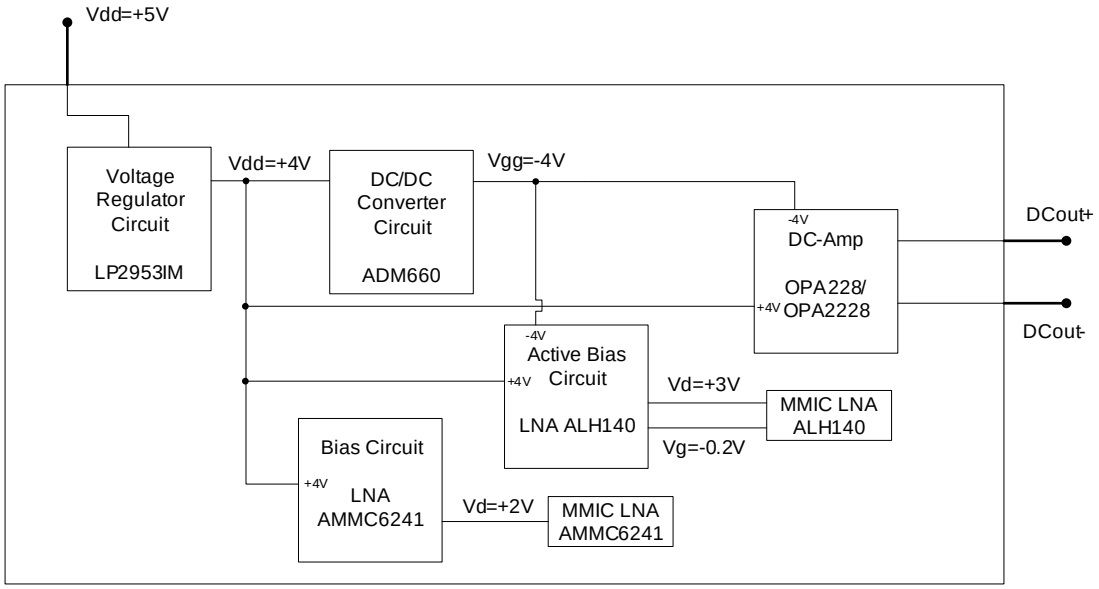

Fig. 7.30. BEM DC circuitry block diagram.

The performance of the LNAs is dependent on the ambient temperature. Since the ALH140 LNA provides a gate bias terminal then an active bias circuit is designed using a PNP bipolar transistor to compensate moderate temperature variations.

All the previous subcircuits are assembled in an aluminium module. The module RF cavity is designed with special care to avoid propagation of higher order modes. The

module is gold-over-nickel plated with 6 μm of nickel, and 3μm of gold (99.9% Au, 0.1% Co). The final assembly of one BEM branch is shown in Fig. 7.31.

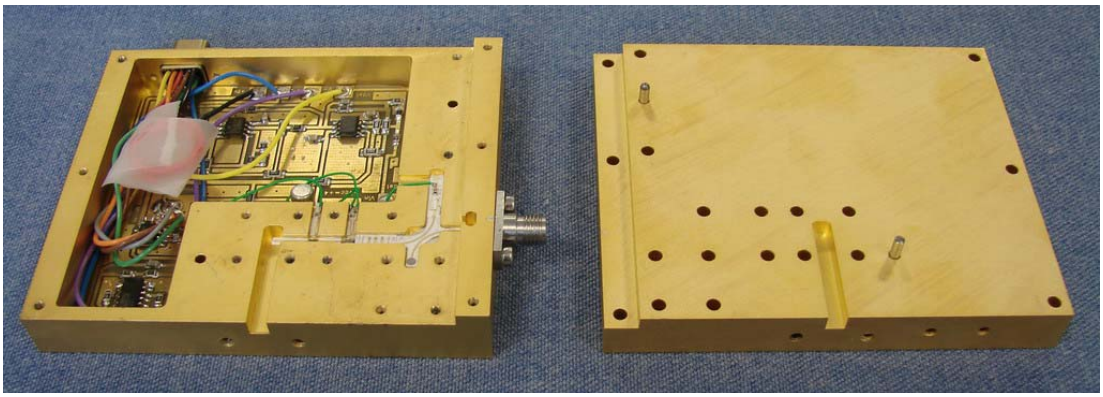

(a)

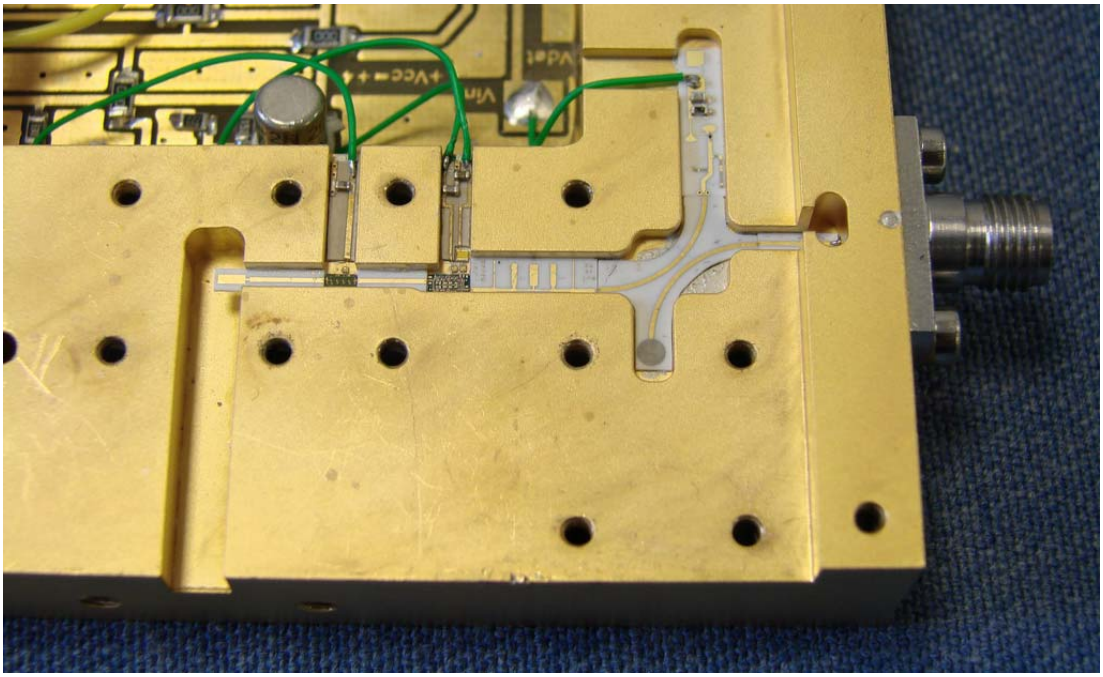

(b)

Fig. 7.31. Pictures of the finished BEM branch; (a) general view with the cover removed, dimensions are 86x71x22 mm^3; (b) detailed view of the RF chain.

For the characterization of the BEM three different measurements are taken: first, the high frequency performance is investigated through an S-parameters measurement between the WR28 input port and the coaxial output port; second, the noise is characterized between the same ports; and finally, the RF to DC conversion is measured both versus frequency and versus input power.

For the measurements the BEM is biased with V_{dd} = 5 V and I_{dd} = 141 mA then the total power consumption is 705 mW per branch. The bias circuits are configured to bias the first LNA with V_{dd} = 2 V and I_{dd} = 58 mA, which minimize its noise

contribution, and the second LNA with V_{dd} = 3 V and I_{dd} = 55 mA. The remaining current is drawn to the DC circuits. The gain results presented in Fig. 7.32a take into account the coupling factor of the directional coupler and hence the measurement is corrected. In the noise measurement there is need to include a waveguide-to-coaxial transition at the BEM input; the noise contribution of this transition is not discounted from the result presented in Fig. 7.32b. The mean noise temperature in the 26.5 – 36 GHz bandwidth is 323.8 K, which is well below the project specification given in Table 7.2.

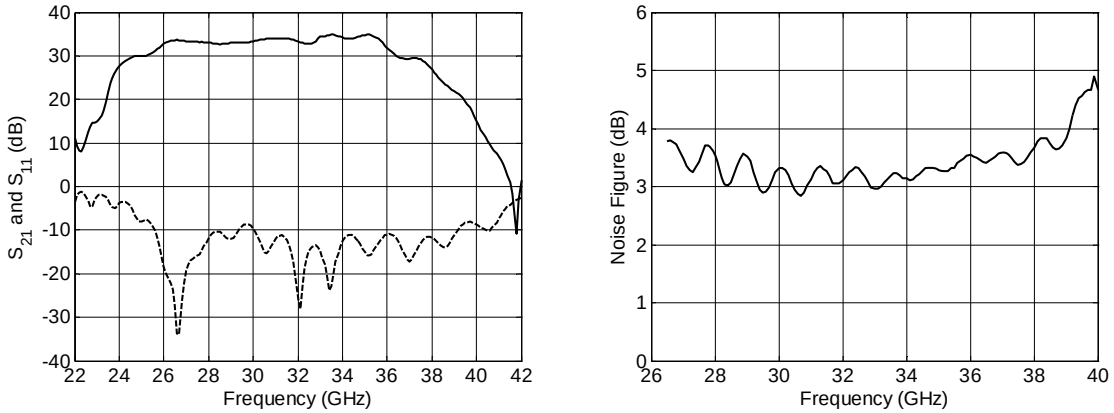

Fig. 7.32. RF and noise results of the BEM branch; (a) Gain (solid line) and WR28 input return loss (dashed line); (b) Noise figure. Gain results are corrected with the coupling factor of the directional coupler. Noise results include a waveguide-to-coaxial input transition.

The RF to DC response is presented in Fig. 7.33 versus input frequency and power. From the data of Fig. 7.33a and (7.2) the BEM effective bandwidth is calculated obtaining a value of 13.1 GHz, which is well above of the required 10 GHz. Finally, the BEM linearity is shown in Fig. 7.33b. The 1 dB compression point is -49 dBm, therefore if the FEM provides the expected power the system would be working in its linear range. The different circuits within the BEM have been investigated regarding the compression and it is found that the detector is the first circuit to compress.

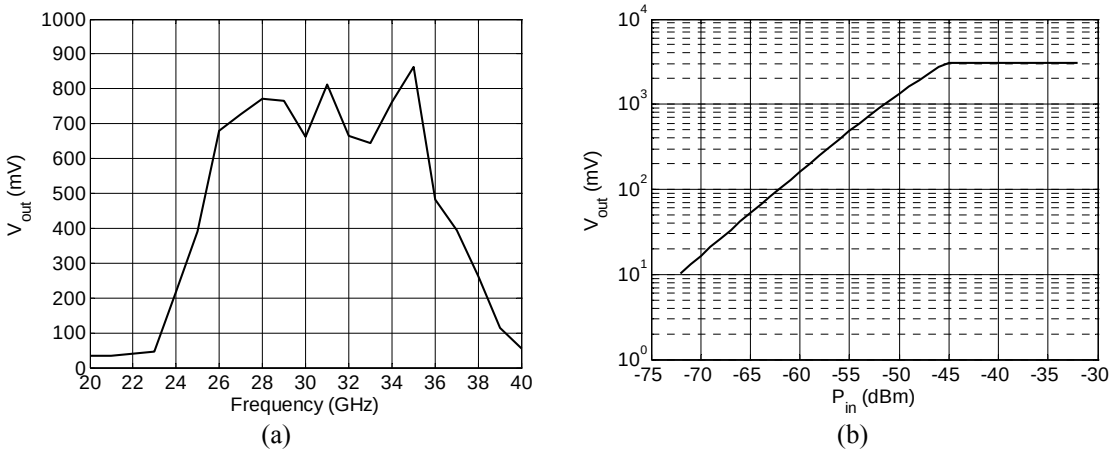

Fig. 7.33. RF to DC BEM performance; (a) Output voltage versus input frequency with an input power of -53 dBm (expected from FEM); (b) Output power versus input power at an input frequency of 31 GHz.

7.3. Conclusions

This chapter has dealed with one of the main applications of the circuits discussed in this thesis: the radiometers. These receivers are used for many applications and hence different configurations have been considered in a short introduction.

Then, the chapter focused in the radiometer for the QUIJOTE project aimed for characterizing the CMB polarization. In this project the DICOM has been involved in the design of different subcircuits which are presented along this chapter. First, it is shown the polar modulators, which are designed in a waveguide configuration to enable fast rotation and thus to eliminate sensitivity limitations related with radiometer gain fluctuations. Then, the orthomode transducers that extract orthogonal linear polarizations from the incoming signal are discussed. Finally, the back-end modules of the 26 – 36 GHz band are detailed. Although the BEM presented in this chapter is for operating at room temperature the design could be optimized for cryogenic operation. Moreover, the MMIC LNA designed in Chapter VI could be used in the BEM amplification stage for room temperature or cryogenic operation.

All the presented subcircuits fulfil the project requirements and hence the techniques, technologies and procedures applied along this thesis are validated to produce final application systems related with microwaves and cryogenics.